APPLIED SCIENCES AND ENGINEERING

Electronic trap detection with carrier-resolved photo-Hall effect

Oki Gunawan[1]*†, Chaeyoun Kim[2]†, Bonfilio Nainggolan[1,3], Minyeul Lee[2], Jonghwa Shin[2], Dong Suk Kim[4,5], Yimhyun Jo[4], Minjin Kim[4], Julie Euvrard[6], Douglas Bishop[1], Frank Libsch[1], Teodor Todorov[1], Yunna Kim[2], Byungha Shin[2]*

Electronic trap states critically affect the performance of semiconductor devices such as transistors, memory devices, and solar cells. Yet, conventional trap measurement techniques often require junction fabrication, which can introduce or alter traps. We present a unique photo-Hall–based method to characterize trap density and energy levels while concurrently extracting charge carrier properties. By analyzing photo-Hall conductivity versus electrical conductivity under varying light intensities and temperatures, we uncover an astonishingly simple hyperbola relationship that reveals detailed charge transport and trap occupation and applied it in silicon and halide perovskite films. This technique substantially expands Hall effect–based measurements by integrating electric, magnetic, photon, and phonon excitations into a single framework and enables unparalleled extraction of charge carrier and trap properties, offering a powerful tool for semiconductor characterization and device optimization.

INTRODUCTION

The performance of semiconductor devices across a wide range of applications can be affected by the presence of trap states. Traps in semiconductors originate from defects or impurities that capture and release free charge carriers. The effect of the traps can modify or dominate the electrical transport and charge carrier recombination process in many devices, often reducing conductivity or decreasing charge carrier lifetime. Traps can also give rise to hysteresis, noise in electrical screening, or electrical leakage and unwanted power dissipation. The sources of traps include impurities and crystalline defects (1) such as point defects, extended defects (dislocations, grain boundaries, and stacking fault), surface states, and interface states. Understanding and controlling these traps is crucial for optimizing the performance of semiconductor devices. The origin and passivation of trap states has been extensively studied in silicon-based materials but continues to be an area of focus in optoelectronic devices such as solar cells and light emitting diodes, as well as in small channel devices where interface states dominate transport. In other material systems, trap states are less explored but equally important. In particular, lead-halide perovskite systems have shown great promise for optoelectronic applications such as solar cells, recently surpassing the record power conversion efficiency of 26.7% in single-junction configurations (2–5). The material system has shown inherently low trap density, enabling their high performance; however, managing and further reducing residual traps is increasingly critical for further performance improvements (6, 7).

Techniques to detect traps in semiconductors include deep-level transient spectroscopy (DLTS) (8, 9), drive-level capacitance profiling (10, 11), space charge–limited current (12, 13), thermal admittance spectroscopy (14, 15), transient photoluminescence (16), time-resolved microwave conductivity (17), photo-Hall spectroscopy (18), transient (19), and constant light photo-Hall effect (20). Each technique offers unique advantages tailored to different aspects of trap properties measurement and suffers from some limitations. See the section SE for a summary. In this study, we present a technique based on recently developed carrier-resolved photo-Hall (CRPH) effect (21) that addresses the major drawbacks of existing approaches including the need for a *p-n* or Schottky junction, the impact of interfaces associated with such device, and the transient nature of most measurements. This new carrier and trap–resolved photo-Hall (CTRPH) technique also provides access to a rich set of charge carrier parameters of up to 17 charge carrier parameters that can be mapped against varying light intensities, including the electron and hole mobilities, photocarrier and trapped carrier density, recombination lifetimes, and diffusion lengths; four parameters associated with the dominant trap state (density, energy level, and scattering cross sections). See section SC for a complete list and descriptions.
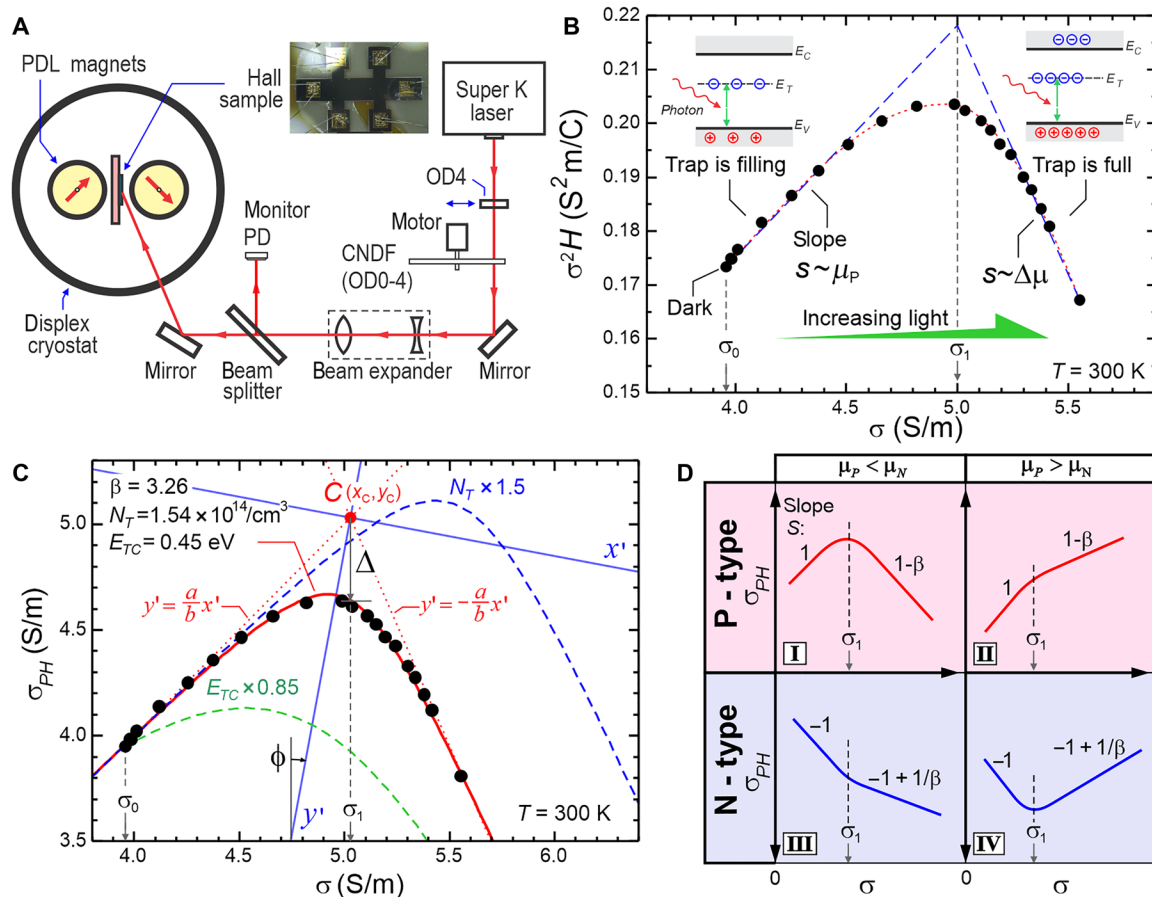
RESULTS

The experiment

The experimental setup is shown in Fig. 1A. The Hall sample is mounted inside a cryostat with temperature control ranging from 20 to 340 K. The sample is placed between two rotating parallel dipole line (PDL) magnets that generate a strong perpendicular oscillating magnetic field (22, 23) with peak amplitude of $B \sim 0.5$ T. We use a supercontinuum white laser that passes through a monochromator and a set of optics to control light intensity and beam size. To demonstrate our trap detection technique, we use a p-type silicon-on-insulator (SOI) sample on glass with thickness $d = 5.0$ μm. The device is a six-terminal Hall bar (see Fig. 1A, inset). The detailed experimental setup and sample fabrication are described in Materials and Methods. The experiment on p-SOI sample represents a photo-Hall experiment in low-injection regime, and later, we will also present data on perovskite sample that represents a high-injection regime.

[1]IBM T. J. Watson Research Center, Yorktown Heights, NY 10598, USA. [2]Dept. of Materials Science and Engineering, Korea Advanced Institute of Science and Technology, Daejeon 34141, Republic of Korea. [3]Dept. of Physics, Arizona State University, Tempe, AZ 85287, USA. [4]Ulsan Advanced Energy Technology R&D Center, Korea Institute of Energy Research, Ulsan 44776, Republic of Korea. [5]Graduate School of Carbon Neutrality, Ulsan National Institute of Science and Technology, Ulsan 44919, Republic of Korea. [6]Dept. of Physics and Centre for Processable Electronics, Imperial College London, London SW7 2AZ, UK.
*Corresponding author. Email: ogunawan@us.ibm.com (O.G.); byungha@kaist.ac.kr (B.S.)
†These authors contributed equally to this work.

Fig. 1. Electronic trap detection with CTRPH technique. (**A**) The experimental setup based on rotating PDL magnet Hall system with cryostat. PD is photodetector, OD is optical density filter, and CNDF is continuous neutral density filter. Inset: the p-type SOI Hall sample. (**B**) The photo-Hall experiment plot of $\sigma^2 H$ versus σ in a p-type SOI sample with laser light of wavelength $\lambda = 615$ nm, maximum intensity $I_L = 157$ mW/cm^2, and temperature $T = 300$ K. The dashed curve is only a guide to the eye. (**C**) Hyperbolic fit (red curve) of the data in Fig. 1B. The x'-y' is the principal axis of the hyperbola centered at point C. The values of fit parameters β, N_T, and E_{TC} are indicated. The impact of varying N_T and E_{TC} are simulated in the blue and green dashed-curve, respectively. (**D**) Four possible scenarios (marked as quadrant I-IV) of photo-Hall behavior with trapping effect depending on carrier type (P or N) and the relative value of the hole and electron mobility. The dashed lines separate the first and second regime of the curves.

The measurement is similar to previously demonstrated CRPH technique (*21*)—In brief, we measure the electrical conductivity σ and Hall coefficient H with increasing light intensity and plot $\sigma^2 H$ versus σ (*21*) as shown in Fig. 1B. In our previous work (*21*), we demonstrated that the minority and majority carrier mobilities can be extracted from the slope $s = d(\sigma^2 H)/d\sigma$, which yield the difference between the hole and electron mobility, i.e., $s = \Delta\mu_H = r(\mu_P - \mu_N)$, where r is the Hall scattering factor and is assumed to be ~1 (*24*). This model applies when the trapping effect is negligible (as in high-quality materials or high light intensity), allowing us to assume that the electron and hole photocarrier density are equal ($\Delta n = \Delta p$). If we extend this model by considering trapping effect, where all the minority carriers are trapped, we show that the slope will yield the majority carrier mobility μ_0 i.e. $s \sim \mu_0$ (see section SA.1 for derivation).

The key insight of the trap detection using CTRPH technique can be seen in the $\sigma^2 H - \sigma$ trace where there is a bending that demarcates two regimes of the plot with positive and negative slope at low and high light intensity, respectively. If we draw two asymptotic

lines as shown in Fig. 1B, we obtain slope of $s = 440$ and -990 cm^2/Vs, respectively, which is consistent with the known mobility values of hole (the majority carrier) in silicon: μ_P ~500 cm^2/Vs and the mobility difference $\Delta\mu = \mu_P - \mu_N$ ~1000 cm^2/Vs (*1*). We can understand this behavior by considering trapping effect of the minority carrier as shown in Fig. 1B (inset). At low light intensity, the photo-generated minority carriers initially populate the traps, and only free photo-generated majority carriers (Δp) contribute to the conductivity, thus $s \sim \mu_P$. Once all the traps are filled at a certain light intensity, the photo-generated minority carriers (Δn) will populate the conduction band (CB) and start contributing to the conductivity. In the limit where the photo-generated carrier density Δn and Δp are much higher than the trap density N_T, we obtain $\Delta n \sim \Delta p$ and $s \sim \Delta\mu_H$ as observed in our earlier study where trapping effects are negligible (*21, 25*).

Theoretical model

We now proceed to a more quantitative analysis of the trap properties. To describe the photo-Hall effect in the presence of traps, we

model a single-level trap in a P-type material with density N_T and energy E_T, which is closer to CB, thus acting as minority carrier trap (see section SA.1). As the light intensity is increased, the electron quasi-Fermi level increases and the trapped (n_T) and free (Δn) electron density can be calculated. To simplify our analysis, we define a new quantity: $\sigma_{PH} = \sigma^2 H / r\mu_0$, which we refer to as "photo-Hall conductivity," and shares the same dimension as σ. We can show that the $\sigma^2 H$ versus σ plot in the presence of traps can be described by a simple hyperbola equation (see section SA.2 for derivation)

$$\frac{\sigma_{PH}'^2}{a^2} - \frac{\sigma'^2}{b^2} = 1 \quad (1)$$

where (σ', σ_{PH}') are (σ, σ_{PH}) expressed in a second coordinate system x'-y', which is centered at point C and rotated by angle ϕ as shown in Fig. 1C. We have $\phi = \frac{1}{2}\tan^{-1}(2/\beta - 1)$, where $\beta = \mu_N / \mu_P$ is the electron-to-hole mobility ratio. To describe the hyperbola equation parameters, we define another two parameters: $s_N = e\mu_0(p_0 + N_T)$ and $s_E = e g_T \mu_0(1 + \beta) N_C \exp(-\varepsilon_{TC})$ where $\varepsilon_{TC} = E_{TC}/k_B T$, with $E_{TC} = E_C - E_T$, E_C is the CB edge, e is the electron's charge, p_0 is the majority carrier density in the dark, N_T is the trap density, g_T is trap energy level degeneracy, which can be assumed to be equal to 1 for deep level traps (26), N_C is the CB effective density of states, k_B is the Boltzmann constant, and T is the temperature. The parameter s_N and s_E have clear physical and geometrical meaning: s_N depends on N_T and determines the horizontal peak position (σ_1) of the hyperbola; s_E depends on E_T and determines the vertical peak position of the hyperbola or the vertical gap "Δ" from the center point C (see Fig. 1C). They are related as $s_E = \Delta^2 / e\beta^2 \mu_0 N_T$.

The hyperbola has a center point, C, which plays a crucial role in this model by automatically providing straightforward solutions for trap density (N_T) and energy level (E_T). The center point C has coordinate $x_C = s_N - s_E$ and $y_C = s_N + (\beta - 1)s_E$. We also have a and b as the hyperbola semimajor and minor axis, respectively, where $a = \sqrt{-K/\lambda_-}$ and $b = \sqrt{K/\lambda_+}$, with $K = e\mu_0\beta^2 N_T s_E$ and $\lambda_\pm = \left(\beta - 2 \pm \sqrt{2\beta^2 - 4\beta + 4}\right)/2$ as the eigen values of the hyperbola matrix (see section SA.2). We note a special case when $\beta = 2$, we have $\phi = 0$, or in other words, the hyperbola x'-y' axes are already aligned with the original $\sigma - \sigma_{PH}$ axes, thus no rotation is needed. From Eq. 1, we can also express σ_{PH} explicitly as a function of σ (see section SA.1)

$$\sigma_{PH}(\sigma) =$$
$$\left[\beta(s_N + s_E) + (2 - \beta)\sigma - \beta\sqrt{(s_N + s_E + \sigma)^2 - 4(s_E\sigma_0 + s_N\sigma)}\right]/2 \quad (2)$$

where σ_0 is the conductivity in the dark. Equation 2 can be used for curve-fitting the experimental data to extract the parameters β, s_N, s_E and thus N_T and E_T. This approach was applied in Fig. 1C, which also presents the resulting fitting parameters.

We note a few important features of the hyperbolic curve as described by Eq. 2. The slope $d\sigma_{PH}/d\sigma$ approaches 1 in the dark at low temperature (or $E_{TC} \gg k_B T$) and 1-β at maximum light intensity. The angle ϕ and the asymptotes $y' = \pm(b/a)x'$ are solely determined by mobility ratio β. The parameters N_T and E_T determine the horizontal and the vertical positions of the inflection (or vertex) point of the hyperbola, respectively. At larger N_T, the inflection point occurs at higher light intensity (or conductivity), as shown in

the blue dashed curve in Fig. 1C where N_T is increased by 1.5×. This shift is expected as more photo-generated carriers are required to fill the traps. Meanwhile, smaller trap energy E_{TC} leads to a smoother hyperbolic curve as shown in the green dashed curve in Fig. 1C, where E_{TC} is reduced to 0.85×. As the impact of the trap on the minority carrier is temperature dependent, shallow traps ($E_{TC} \sim k_B T$) produce smoother hyperbolic curves, while deep traps ($E_{TC} \gg k_B T$) result in sharper hyperbolic curves.

Figure 1D summarizes the expected shape of the $\sigma_{PH} - \sigma$ trace for four possible scenarios (marked as quadrant I to IV) depending on the material types (P or N) and the relative mobility values ($\mu_P < \mu_N$ or $\mu_P > \mu_N$). Our hyperbola model (Eq. 2) applies for all cases, albeit with minor modifications in formula for N-type systems (see section SA.5). This diagram also reveals important characteristics: The slope changes by the mobility ratio of minority to majority carrier, i.e., $-\beta$ or $+1/\beta$ for P-type and N-type, respectively, which implies that significant bending behavior occurs when the mobility ratio is large (e.g., Fig. 1D, quadrant I and IV). This is reasonable because once the trap becomes full and the system enters a second regime, the minority carrier starts contributing to the transport and the change in slope will be significant if the minority carrier mobility is larger than that of the majority. For example, the p-SOI data in Fig. 1C show quadrant I behavior since it is a P-type with $\beta = 3.26$.

DISCUSSION
CTRPH analysis in the p-SOI sample
We can now apply a complete CTRPH analysis to the p-SOI data. We can use two approaches to extract the trap parameters N_T and E_{TC} from the photo-Hall experiment. The first technique would require to fit the experimental data ($\sigma_{PH} - \sigma$) using Eqs. 1 or 2 and extract β, s_N, and s_E as fitting parameters. This curve fitting is illustrated in Fig. 1C, which yields $\beta = 3.26$, $N_T = 1.54 \times 10^{14}$/cm³, and $E_{TC} = 0.45$ eV. The β value is close to 3 as expected for silicon (1). This approach is however hindered by the need for effective mass that appears in the effective density of states N_C (or N_V) in calculation involving s_E, which, while known for many materials, is rarely available for new materials.

In the second technique, which is an alternative to curve fitting, we can perform a geometric analysis of the $\sigma_{PH} - \sigma$ trace to extract β, N_T and E_{TC}. β is extracted from the slope of the high light intensity regime with the asymptotic limit of 1-β and calculated using $\beta = 1 - (d\sigma_{PH}/d\sigma)_\infty$. Note that β is however not required to calculate N_T and E_{TC}. When $E_{TC} \gg k_B T$, which can be achieved at low temperature, the hyperbola becomes sufficiently sharp, and the trap density can be estimated with a very simple equation (see section SA.3)

$$\tilde{N}_T = \frac{\sigma_1 - \sigma_0}{e\mu_0} \quad (3)$$

where $\tilde{N}_T$ is the estimated trap density calculated from the difference between the inflection (or vertex) point at σ_1 and the dark conductivity σ_0 as shown in Fig. 1C. The difference in conductivity between the point σ_1 and σ_0 is primarily due to free majority carriers (Δp). As all available trap states are filled by the photo-generated electrons near the inflection point of the hyperbola, the Δp at this point is close to the trap density N_T. A more exact expression of Eq. 3 that contains temperature correction is given in section SA.3.

Next, we can determine the trap energy E_{TC} by measuring the gap Δ in Fig. 1C and use the relationship (see section SA.4 for derivation)

$$E_{TC} = k_B T \ln\left[e^2 g_T \mu_0^2 \beta^2 (\beta+1) N_C N_T / \Delta^2 \right] \quad (4)$$

In this example, we have $\Delta = 0.462$ S/m and thus $E_{TC} = 0.46$ eV, consistent with direct curve-fitting technique in Fig. 1C. In addition, we can also perform variable temperature photo-Hall measurements, which can provide more accurate access to E_{TC} without the need for prior knowledge of effective mass or the center point C. We demonstrate that the slope $S_0 = \left[d\sigma_{PH}/d\sigma\right]_0$ at the dark point is related to E_{TC} according to (see section SA.4)

$$\ln\left(\frac{1-S_0}{(\beta+S_0-1)(1+\beta)T^{1.5}} \right) = c_0 - \frac{E_{TC}}{k_B T} \quad (5)$$
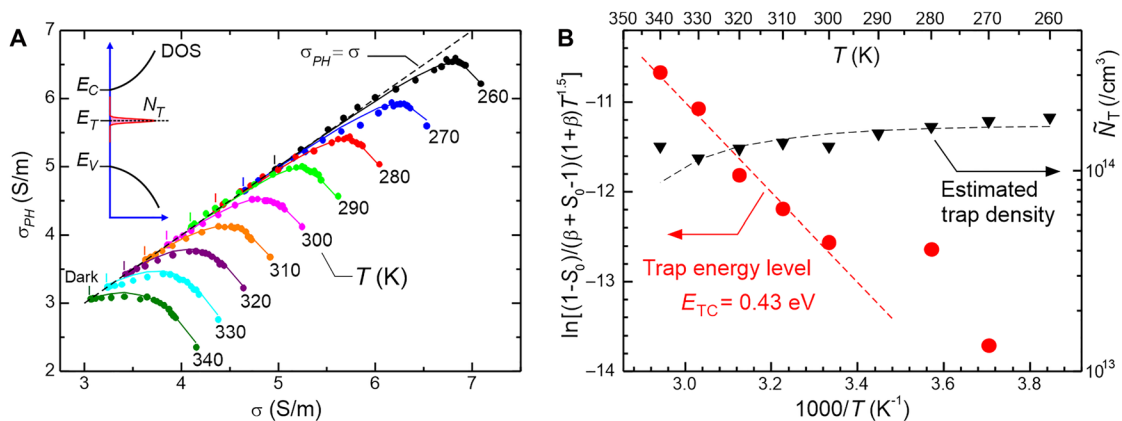
where c_0 is a constant. Here, we rely on the fact that the slope S_0 drops significantly toward higher temperature as shown in Fig. 2A. We can perform an Arrhenius analysis by plotting the left hand–side quantity versus $1/T$ and extract E_{TC} from the slope. We apply this variable temperature approach to the photo-Hall measurements of the p-SOI sample at $T = 260$ to 340 K as shown in Fig. 2. We observe that all curves show hyperbolic behavior and become sharper at lower temperature or $E_{TC} \gg k_B T$. The first segment of the curve approaches asymptotic limit $\sigma_{PH} = \sigma$ toward low temperature as expected from the theory. We obtain trap density $N_T = 1.66 \times 10^{14}$ /cm^3 from the hyperbola peaks and using Eq. 3 at low temperature range ($T \sim 260$ K). This value is close to $N_T = 1.54 \times 10^{14}$ /cm^3 determined from curve-fitting approach in Fig. 1C. We also observe in Fig. 2B that the $\tilde{N}_T$ values drop slightly at higher temperatures, which is consistent with the theoretical prediction (indicated as black-dashed curve) described in section SA.3. In general, the trap density N_T can be more accurately determined at lower temperature as the hyperbola curve becomes sharper.

Using Eq. 5, we extract E_{TC} from the slope of the data in Fig. 2B. A linear behavior with respect to $1/T$ is observed at high temperature range (300 to 340 K), the slope yields $E_{TC} = 0.43$ eV. At low temperature ($T < 300$ K), the slope S_0 approaches 1, and the left hand–side quantity of Eq. 5, which contains 1-S_0, becomes less

accurate and noisier (Fig. 2B). Therefore, the data in this low-temperature range can be excluded. This E_{TC} value is very close to the value obtained from previous technique using curve-fitting or Δ calculation, i.e., (0.45 eV). Some discrepancy from the first method can be attributed to inaccuracy of point C determination (that relies on intersection of two asymptotes) and the value of the effective mass of the SOI sample (which could change under strain). Nevertheless, close and consistent results of N_T and E_{TC} demonstrate the reliability of both approaches. We note that similar trap level of 0.48 eV has been previously observed in SOI samples using DLTS study, and the trap is suspected because of small voids from poorly bonded SOI ([27]).

From Fig. 2, we observe a contrasting trend: N_T and E_{TC} can generally be determined more accurately at low and high temperatures, respectively. At low temperatures, the hyperbola becomes sharper, allowing its peak position (σ_1)—used to calculate N_T in Eq. 3—to be determined with higher precision. In contrast, determining E_{TC} relies on significant variation in the slope S_0, which occurs at higher temperatures. Thus E_{TC} can be more accurately determined at higher temperature range.

To complete the analysis of the SOI sample, we extend our CTRPH analysis in similar fashion with our previous work ([21]), but now incorporating the presence of traps (see section SB). This approach enables us to fully resolve the concentration of electrons in the trap (n_T), electron photocarrier density (Δn), and hole photocarrier density (Δp) using $n_T = \left[(\beta-1)\sigma + \sigma_{PH} - \beta\sigma_0\right] / e\mu_P\beta$, $\Delta n = (\sigma - \sigma_{PH}) / e\mu_P\beta(\beta+1)$, and $\Delta p = \Delta n + n_T$ (see section SA.1). Consequently, we can now calculate up to $17 \times N$ charge carrier parameters, where N represents the number of light intensity settings. A complete list is provided in section SC. The electron and hole charge carrier parameters include photo carrier densities (Δn and Δp), occupied trap density (n_T), mobility (μ_N and μ_P), recombination lifetime (τ_N and τ_P), diffusion coefficients (D_N, D_P, and D_A), and diffusion lengths ($L_{D,N}$, $L_{D,P}$, and $L_{D,A}$), where the subscript N, P, and A means electron, hole, and ambipolar quantity, respectively. Given the carrier density information, we can also calculate quasi-Fermi levels (QF_N and QF_P), their splitting ($QFLS$) and its ideality factor (η) as suggested in ([20]). In addition, we can extract four trap parameters, including trap density N_T, trap energy E_{T}, and

Fig. 2. Trap analysis using temperature-dependent CTRPH measurement in the p-SOI sample. (**A**) Photo-Hall data from $T = 260$ to 340 K with laser light of $\lambda = 550$ nm and maximum intensity $I_L = 165$ mW/cm^2. The dark data points are indicated by short vertical dashes. The dashed line is the $\sigma_{PH} = \sigma$ asymptotic line. Inset: energy band diagram of the trap model. (**B**) Arrhenius plot of Eq. 5 to extract the trap energy level (E_{TC}) and the estimated trap density ($\tilde{N}_T$) extracted using Eq. 3. Black dashed-curve: curve-fit of temperature-dependent effect of ($\tilde{N}_T$) (see text).

recombination scattering cross sections (σ_P and σ_N). The complete extraction of these parameters, along with relevant plots for the p-SOI sample, is presented in section SD.2.
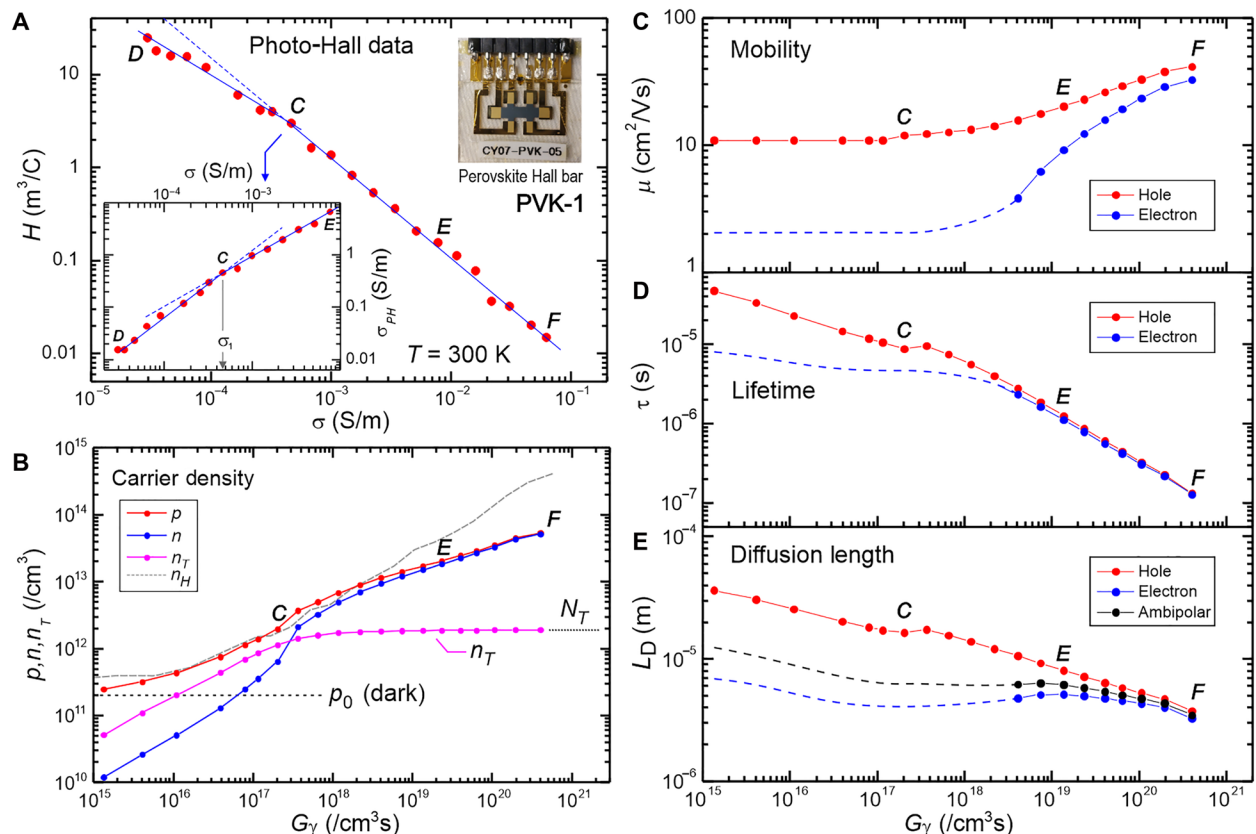
We have also demonstrated CTRPH analysis in an N-type silicon sample as detailed in section SD.3. The data exhibit broad hyperbola or quadrant III (Fig. 1D) behavior in. From the second segment, we obtain the slope $S = -1 + 1/\beta = 0.691$, which yield $\beta = 3.24$ and thus hole (minority) mobility of $\mu_P = \mu_N/\beta = 526\ cm^2/Vs$. We note that, again, both mobilities are consistent with the known values in silicon of $\mu_P \sim 500$ and $\mu_N \sim 1500\ cm^2/Vs$ (1), similar to the results from the p-SOI sample. From the inflection point, we obtain trap density $N_T = 2.5 \times 10^{12}/cm^3$. For the trap energy level, because of weak bending near the inflection point, we cannot determine the parameter Δ accurately. However we can establish its upper limit, i.e., $\Delta < 9.4 \times 10^{-4}\ S/m$ and thus the upper bound of the trap energy using Eq. 4, i.e., $E_{TV} < 0.55\ eV$. The full set of CTRPH analysis plots, including carrier density, quasi-Fermi levels, mobility, lifetime, diffusion lengths, and ideality factors, are presented in fig. S6.

CTRPH analysis in perovskite
We further apply the CTRPH technique to a high-performance FAPbI$_3$ perovskite photovoltaic film, processed identically to the perovskite layers used in solar cell devices that recently achieved a record power conversion efficiency of 25.4% (28). The sample is a six-terminal Hall bar on glass with thickness $d = 0.7\ \mu m$. The sample demonstrates a CTRPH trap analysis in a unique context where (i) $\mu_P > \mu_N$ (Fig. 1D, quadrant II), (ii) a high injection regime ($\Delta p \gg p_0$), and (iii) variable mobility at high light intensity. To address these characteristics, the analysis is divided into two regimes: trapping regime (indicated by data point range D-C-E in Fig. 3A) and high light intensity where the mobility may vary (range E to F). We observe that the perovskite data exhibit broad hyperbola or quadrant II behavior as shown in Fig. 1D where $\mu_P > \mu_N$, i.e., the minority (electron) mobility is less than that of majority (hole). The hyperbola appears broad because, at high light intensity (in the second segment), the minority carrier begins to contribute to the transport, but its contribution is small and only slightly changes the slope.

From the inflection point C in Fig. 3A (inset), we determine the trap density: $N_T = 3.7 \times 10^{12}/cm^3$ using Eq. 3, which is ~30× smaller than Δn or Δp at maximum light intensity (see Fig. 3B). Notably, this N_T value is significantly below the detection limit of junction capacitance–based trap extraction methods ($N_{T,min} \sim 10^{15}/cm^3$ at $d = 0.7\ \mu m$) (7, 29), underscoring the advantage of this technique. This measurement also shows that this perovskite film has trap density on par with single crystal type (7) consistent with its high photovoltaics performance. The hyperbola curve profile is however too smooth to confidently determine the gap Δ and the trap energy level, but we estimate $E_{TC} \sim 0.3$ to $0.7\ eV$.

Fig. 3. CTRPH trap analysis of a high-performance FAPbI$_3$ perovskite film "PVK-1." (**A**) The photo-Hall data with laser light $\lambda = 615\ nm$ and maximum intensity $I_L = 16\ mW/cm^2$. Points D, C, and F mark the dark, inflection point, and full light intensity, respectively. Bottom inset: σ_{PH}versus σ data that show bending behavior due to trap. Top inset: the perovskite Hall bar sample. (**B**) Carrier density versus absorbed photo density (G_γ). $n_H = 1/eH$ is the Hall density for comparison. (**C**) Mobility. (**D**) Recombination lifetime. (**E**) Diffusion length. Dashed curves in (C) to (E) are estimated minority carrier values as the minority mobility values between dark and inflection point C are more uncertain.

In the high light intensity regime, we obtain self-consistent solutions using an iterative technique for intensity-dependent mobility, as described in our previous work (21) (see also section SD.4 for more detailed analysis). The extracted parameters are displayed as a function of absorbed photon density G_γ in Fig. 3 (B to E). We observe that this perovskite sample exhibits excellent charge carrier parameters ($\mu \sim 40$ cm^2/Vs, $\tau \sim 100$ ns and $L_D \sim 3$ μm) at maximum light intensity of ~0.16 sun, along with a very low trap density N_T. This is consistent with the recent record performance of the associated solar cell device (28).

We note another aspect of this work: Our technique uses a simple model that assumes a single dominant trap with a narrow energy level. In practice, multiple traps or more complex situations—such as distributed traps, tail states, or Urbach tail—may exist, accompanied by a distribution of carrier mobilities. Nevertheless, we expect a qualitatively similar behavior to the single-level model, in which the σ_{PH} versus σ plot still consists of two segments corresponding to the trap-filling and trap saturated regime, which may not be exactly a hyperbola. For example, in the case of multilevel traps, we expect that the behavior of the corresponding σ_{PH} versus σ trace at a given temperature will be dominated by the deepest trap level which is partially filled. Therefore, if the trap energy levels are well separated, and we observe a hyperbola-like plot, we could use the single-level trap extraction formulas to obtain features of a multilevel trap distribution. These cases will be investigated in more detail in the future.

In summary, we have demonstrated a comprehensive approach for extracting trap and charge carrier properties from semiconductors using the CTRPH technique, which relies on a detailed analysis of the σ_{PH} versus σ curve, whose underlying behavior follows a newly derived hyperbola equation. This work provides a unified framework for gaining deeper insights into charge carrier transport and trapping effects by using the most common excitations: electric field, magnetic field, photon (light), and phonon (via lattice temperature control) based on the Hall effect. Beyond traditional electric and magnetic field applications in Hall measurements, increasing photon intensity allows us to fill traps, determine their density, and evaluate the mobility ratio of the charge carriers. By varying temperature or phonon excitation, we probe the trap energy levels. This technique significantly enhances the capabilities of Hall effect measurements and holds potential for broad application, enabling single-experiment, comprehensive evaluation of charge carrier transport and trap properties in many emerging advanced electronic materials.

MATERIALS AND METHODS
Experimental setup
The setup is shown in Fig. 1A. The PDL Hall system consists of a dry cryogen–free displex cryostat system with a custom-built cold stage equipped with a 50-W resistive heater, enabling temperature control from 20 to 340 K using a Lakeshore 340 temperature controller. The fundamental operation of the PDL Hall system is detailed in (21–23). The sample is mounted on the cold stage, positioned between two rotating PDL magnets made of NdFeB, each measuring 25.4 mm in diameter and 25.4 mm in length. The magnetic field applied to the sample is $B = \pm 0.5$ T.

Light illumination is provided by either a red-green-blue (RGB) laser or supercontinuum white laser (Super K Fianium FIU-15 from NKT Photonics) equipped with monochromator system. Light intensity is controlled over eight orders of magnitude using a combination of a continuous neutral density filter (CNDF) and optical density 4 (OD4) filter. The CNDF is driven by a stepper motor and the OD4 filter is driven by a two-position motorized flipper. A series of biconvex and biconcave lenses expand the beam to obtain ~10-mm coverage diameter to ensure uniform illumination of the entire Hall sample. The light beam is split by a beam splitter, with one part directed downward to a "monitor photodetector" for real-time intensity monitoring and the other is directed at the sample.

The electronic instrumentation system consists of a Keithley 2450 source meter unit for providing current or voltage to the sample, a Keithley 2182A nanovoltmeter for measuring longitudinal and transverse voltage across the Hall sample, and a Keithley 6485 picoammeter to measure photocurrent or light intensity via the monitor photodetector or the reference photodetector cell. We have also built a custom PDL electronic control box that contains Raspberry Pi (RPi) Compute Module 4 microcomputer, a four-channel stepper motor controller (EZ4AXIS23WV from AllMotion), Pi-Plate data acquisition boards with analog and digital I/O mounted on top of the RPi, and custom-designed Hall effect switch matrix unit. This high-input impedance switch matrix (capable of resistance measurements up to 1 TΩ) features six sample input channels, two source input channels, and two voltage read-out channels, allowing simultaneous measurements of longitudinal (R_{xx}) and/or transverse (R_{xy}) resistance.

The stepper motor controller controls the rotation of the PDL magnets, the CNDF, and a linear stage for switching between the RGB laser and the Super K laser. The RPi microcomputer functions as a server, controlling operations of various modules inside the box. The box is controlled by a client Windows computer that runs MATLAB programs to execute various measurement operations.

Fabrication of SOI Hall samples
The sample is an intrinsic SOI wafer, consisting of a 5-μm single-crystalline intrinsic Si device layer, a 500-nm SiO$_2$ layer, and a 525-μm Si handle layer. To transfer this single-crystalline Si film onto a SiO$_2$ substrate, the SOI wafer was bonded to a 500-μm-thick borosilicate glass using a fusion bonding process at 673 K and a pressure of 1.5 kN. Subsequently, the unwanted handle layer was removed via chemical mechanical polishing process, and residual Si was etched using a SF$_6$ dry etch process. The remaining 500 nm SiO$_2$ layer was then chemically etched with HF solution, yielding the single-crystalline Si film on the SiO$_2$ substrate wafer. This Si/SiO$_2$ wafer was then diced into 10 mm–by–10 mm pieces, and a photolithography process was used to form a Hall bar photoresist pattern on the Si film. The Si Hall bar was then created using SF$_6$ dry etching, followed by photoresist removal. Last, 200-nm-thick Au electrodes were deposited on the Hall bar using an e-beam evaporator. The SOI Hall bar sample was mounted on a custom-made sample printed circuit board (PCB) package using "GE" varnish, and the Hall bar contacts were wire-bonded to the PCB pads. For variable temperature photo-Hall measurements, a small diode temperature sensor was attached to the glass substrate to accurately monitor the sample's temperature.

Fabrication of perovskite Hall samples
The perovskite Hall samples are based on formamidinium-rich lead iodide (FAPbI$_3$) films with methylammonium chloride (MACl) additives. This high-quality perovskite exhibits a solar cell device power conversion efficiency of 25.7% and has a bandgap of 1.55 eV as reported in (28, 30). Following these reports, FAPbI$_3$ black powder

was synthesized by first dissolving PbI_2 and FAI in a 1:1 molar ratio in 2-methoxyethanol (0.8 M), and then filtered using a polyvinylidene fluoride filter with 0.45-μm pore size. The filtered solution was placed in a flask incubated in an oil bath at 120°C for 1 hour with slow stirring. The resulting black powder was filtered using a glass filter and dried at 60°C for 24 hours.

The perovskite precursor solution was prepared by dissolving 1550 mg $FAPbI_3$ and 61 mg MACl with 1 ml of N,N'-dimethylformamide/dimethyl sulfoxide (4:1). The perovskite solution was filtered with a polyvinylidene fluoride filter (0.2 μm), and then 70 μl of the filtered perovskite solution was spread onto the 2.5 cm–by–2.5 cm glass substrate at 8000 rpm rotation speed for 50 s. During spin-coating, 1 ml of diethyl ether was dropped on the perovskite film at 10 s using a homemade pipette. The resulting film was annealed at 150°C for 15 min, followed by 100°C for 30 min on a hotplate, yielding high-quality $FAPbI_3$ film with a thickness of 700 nm.

To perform photo-Hall measurement, a six-terminal perovskite Hall bar device was patterned by scraping away the excess film outside the Hall bar region. A 100-nm-thick Au contact pattern was then deposited on the film. An eight-terminal header pin was attached to the glass substrate with epoxy, and its metal pins were connected to the Au contact pattern using silver epoxy. A small diode temperature sensor was also attached to the sample to monitor its temperature. Since the perovskite thin film is highly sensitive to air and moisture, the Hall bar was encapsulated by attaching a secondary glass cover with epoxy. We attempted the measurements immediately after sample fabrication within a month and stored the samples in nitrogen desiccator box.

Supplementary Materials

This PDF file includes:
Supplementary Text
Figs. S1 to S9
Tables S1 to S5
References

REFERENCES

1. D. K. Schroder, "Ch. 5 Defects" in *Semiconductor Material and Device Characterization* (Wiley, ed. 3, 2005), p. 251, 504.
2. J. Jeong, M. Kim, J. Seo, H. Lu, P. Ahlawat, A. Mishra, Y. Yang, M. A. Hope, F. T. Eickemeyer, M. Kim, Y. J. Yoon, I. W. Choi, B. P. Darwich, S. J. Choi, Y. Jo, J. H. Lee, B. Walker, S. M. Zakeeruddin, L. Emsley, U. Rothlisberger, A. Hagfeldt, D. S. Kim, M. Grätzel, J. Y. Kim, Pseudo-halide anion engineering for α-$FAPbI_3$ perovskite solar cells. *Nature* **592**, 381–385 (2021).
3. J. Park, J. Kim, H.-S. Yun, M. J. Paik, E. Noh, H. J. Mun, M. G. Kim, T. J. Shin, S. I. Seok, Controlled growth of perovskite layers with volatile alkylammonium chlorides. *Nature* **616**, 724–730 (2023).
4. H. Chen, C. Liu, J. Xu, A. Maxwell, W. Zhou, Y. Yang, Q. Zhou, A. S. R. Bati, H. Wan, Z. Wang, L. Zeng, J. Wang, P. Serles, Y. Liu, S. Teale, Y. Liu, M. I. Saidaminov, M. Li, N. Rolston, S. Hoogland, T. Filleter, M. G. Kanatzidis, B. Chen, Z. Ning, E. H. Sargent, Improved charge extraction in inverted perovskite solar cells with dual-site-binding ligands. *Science* **384**, 189–193 (2024).
5. M. A. Green, E. D. Dunlop, M. Yoshita, N. Kopidakis, K. Bothe, G. Siefer, D. Hinken, M. Rauer, J. Hohl-Ebinger, X. Hao, Solar cell efficiency tables (Version 64). *Prog. Photovolt. Res. Appl.* **32**, 425–441 (2024).
6. H. Jin, E. Debroye, M. Keshavarz, I. G. Scheblykin, M. B. J. Roeffaers, J. Hofkens, J. A. Steele, It's a trap! On the nature of localised states and charge trapping in lead halide perovskites. *Mat. Hor.* **7**, 397–410 (2020).
7. J. Siekmann, S. Ravishankar, T. Kirchartz, Apparent defect densities in halide perovskite thin films and single crystals. *ACS Energy Lett.* **6**, 3244–3251 (2021).
8. D. Lang, Deep-level transient spectroscopy: A new method to characterize traps in semiconductors. *J. Appl. Phys.* **45**, 3023–3032 (1974).
9. X. Ren, B. Zhang, L. Zhang, J. Wen, B. Che, D. Bai, J. You, T. Chen, S. Liu, Deep-level transient spectroscopy for effective passivator selection in perovskite solar cells to attain high efficiency over 23%. *ChemSusChem* **14**, 3182–3189 (2021).
10. C. Michelson, A. Gelatos, J. Cohen, Drive-level capacitance profiling: Its application to determining gap state densities in hydrogenated amorphous silicon films. *Appl. Phys. Lett.* **47**, 412–414 (1985).
11. Z. Ni, C. Bao, Y. Liu, Q. Jiang, W. Q. Wu, S. Chen, X. Dai, B. Chen, B. Hartweg, Z. Yu, Z. Holman, J. Huang, Resolving spatial and energetic distributions of trap states in metal halide perovskite solar cells. *Science* **367**, 1352–1358 (2020).
12. R. H. Bube, Trap density determination by space-charge-limited currents. *J. Appl. Phys.* **33**, 1733–1737 (1962).
13. E. A. Duijnstee, J. M. Ball, V. M. Le Corre, L. J. A. Koster, H. J. Snaith, J. Lim, Toward understanding space-charge limited current measurements on metal halide perovskites. *ACS Energy Lett.* **5**, 376–384 (2020).
14. H.-S. Duan, H. Zhou, Q. Chen, P. Sun, S. Luo, T.-B. Song, B. Bob, Y. Yang, The identification and characterization of defect states in hybrid organic–inorganic perovskite photovoltaics. *Phys. Chem. Chem. Phys.* **17**, 112–116 (2015).
15. S. Wang, P. Kaienburg, B. Klingebiel, D. Schillings, T. Kirchartz, Understanding thermal admittance spectroscopy in low-mobility semiconductors. *J. Phys. Chem. C* **122**, 9795–9803 (2018).
16. S. D. Stranks, V. M. Burlakov, T. Leijtens, J. M. Ball, A. Goriely, H. J. Snaith, Recombination kinetics in organic-inorganic perovskites: Excitons, free charge, and subgap states. *Phys. Rev. Appl.* **2**, 034007 (2014).
17. E. M. Hutter, G. E. Eperon, S. D. Stranks, T. J. Savenije, Charge carriers in planar and meso-structured organic-inorganic perovskites: Mobilities, lifetimes, and concentrations of trap states. *J. Phys. Chem. Lett.* **6**, 3082–3090 (2015).
18. A. Musiienko, P. Moravec, R. Grill, P. Praus, I. Vasylchenko, J. Pekarek, J. Tisdale, K. Ridzónová, E. Belas, L. Landová, B. Hu, E. Lukosi, M. Ahmadi, Deep levels, charge transport and mixed conductivity in organometallic halide perovskites. *Energ. Environ. Sci.* **12**, 1413–1425 (2019).
19. Z. Kachwalla, D. J. Miller, Transient spectroscopy using the Hall effect. *Appl. Phys. Lett.* **50**, 1438–1440 (1987).
20. A. Musiienko, F. Yang, T. W. Gries, C. Frasca, D. Friedrich, A. Al-Ashouri, E. Sağlamkaya, F. Lang, D. Kojda, Y.-T. Huang, V. Stacchini, R. L. Z. Hoye, M. Ahmadi, A. Kanak, A. Abate, Resolving electron and hole transport properties in semiconductor materials by constant light-induced magneto transport. *Nat. Commun.* **15**, 316 (2024).
21. O. Gunawan, S. R. Pae, D. M. Bishop, Y. Virgus, J. H. Noh, N. J. Jeon, Y. S. Lee, X. Shao, T. Todorov, D. B. Mitzi, B. Shin, Carrier-resolved photo-Hall effect. *Nature* **575**, 151–155 (2019).
22. O. Gunawan, Y. Virgus, K. Fai Tai, A parallel dipole line system. *Appl. Phys. Lett.* **106**, 062407 (2015).
23. O. Gunawan, T. Gokmen, Hall measurement system with rotary magnet, US patent 9,041,389 (2015).
24. S. M. Sze, K. K. Ng, "Ch. 1 Physics and properties of semiconductors – A review" in *Physics of Semiconductor Devices* (Wiley, ed. 3, 2006), pp. 34–35.
25. J. Euvrard, O. Gunawan, D. B. Mitzi, Impact of PbI_2 passivation and grain size engineering in $CH_3NH_3PbI_3$ solar absorbers as revealed by carrier-resolved photo-Hall technique. *Adv. Energy Mater.* **9**, 1902706 (2019).
26. R. F. Pierret, G. W. Neudeck, "Ch. 4 Equilibrium carrier statistics" in *Advanced Semiconductor Fundamentals, vol. 6* (Addison-Wesley, ed. 2, 1987), p. 120.
27. A. Usami, T. Natori, A. Ito, S.-I. Ishigami, Y. Tokuda, T. Wada, Study of electrical properties of defects in SOI films by wafer bonding. *MRS Onl. Proc. Lib.* **262**, 349–354 (1992).
28. M. Kim, J. Jeong, H. Lu, T. K. Lee, F. T. Eickemeyer, Y. Liu, I. W. Choi, S. J. Choi, Y. Jo, H.-B. Kim, S.-I. Mo, Y.-K. Kim, H. Lee, N. G. An, S. Cho, W. R. Tress, S. M. Zakeeruddin, A. Hagfeldt, J. Y. Kim, M. Grätzel, D. S. Kim, Conformal quantum dot–SnO_2 layers as electron transporters for efficient perovskite solar cells. *Science* **375**, 302–306 (2022).
29. S. Ravishankar, T. Unold, T. Kirchartz, Comment on "Resolving spatial and energetic distributions of trap states in metal halide perovskite solar cells". *Science* **371**, eabd8014 (2021).
30. M. Kim, G. H. Kim, T. K. Lee, I. W. Choi, H. W. Choi, Y. Jo, Y. J. Yoon, J. W. Kim, J. Lee, D. Huh, H. Lee, S. K. Kwak, J. Y. Kim, D. S. Kim, Methylammonium chloride induces intermediate phase stabilization for efficient perovskite solar cells. *Joule* **3**, 2179–2192 (2019).
31. W. Shockley, W. Read Jr., Statistics of the recombinations of holes and electrons. *Phys. Rev.* **87**, 835–842 (1952).
32. R. N. Hall, Electron-hole recombination in germanium. *Phys. Rev.* **87**, 387–387 (1952).
33. R. A. Smith, "Ch. 5 Electron transport phenomena" in *Semiconductors* (Cambridge, ed. 2, 1978), p. 109.
34. I. Levine, S. Gupta, A. Bera, D. Ceratti, G. Hodes, D. Cahen, D. Guo, T. J. Savenije, J. Avila, H. J. Bolink, O. Millo, D. Azulay, I. Balberg, Can we use time-resolved measurements to get steady-state transport data for halide perovskites? *J. Appl. Phys.* **124**, 103103 (2018).
35. Matrix representation of conic sections. Wikipedia, https://en.wikipedia.org/wiki/Matrix_representation_of_conic_sections, accessed Oct 2024.
36. Conic section. Wikipedia, https://en.wikipedia.org/wiki/Conic_section, accessed Oct 2024.
37. A. B. Ayoub, The central conic sections revisited. *Math. Mag.* **66**, 322–325 (1993).

38. Hyperbola. Wikipedia, https://en.wikipedia.org/wiki/Hyperbola, accessed Oct 2024.

39. K. J. Meech, R. Weryk, M. Micheli, J. T. Kleyna, O. R. Hainaut, R. Jedicke, R. J. Wainscoat, K. C. Chambers, J. V. Keane, A. Petric, L. Denneau, E. Magnier, T. Berger, M. E. Huber, H. Flewelling, C. Waters, E. Schunova-Lilly, S. Chastel, A brief visit from a red and extremely elongated interstellar asteroid. *Nature* **552**, 378–381 (2017).

40. H. Yin, A. Akey, R. Jaramillo, Large and persistent photoconductivity due to hole-hole correlation in CdS. *Phys. Rev. Mater.* **2**, 084602 (2018).

41. D. Ompong, K. S. Ram, D. D. Y. Setsoafia, H. Mehdizadeh Rad, J. Singh, Saturation of open-circuit voltage at higher light intensity caused by interfacial defects and nonradiative recombination losses in perovskite solar cells. *Adv. Mater. Interfaces* **10**, 2201578 (2022).

42. P. Caprioglio, M. Stolterfoht, C. M. Wolff, T. Unold, B. Rech, S. Albrecht, D. Neher, On the relation between the open-circuit voltage and quasi-Fermi level splitting in efficient perovskite solar cells. *Adv. Energy Mater.* **9**, 1901631 (2019).

43. Y. Chen, H. T. Yi, X. Wu, R. Haroldson, Y. N. Gartstein, Y. I. Rodionov, K. S. Tikhonov, A. Zakhidov, X.-Y. Zhu, V. Podzorov, Extended carrier lifetimes and diffusion in hybrid perovskites revealed by Hall effect and photoconductivity measurements. *Nat. Commun.* **7**, 12253 (2016).

44. P. Caprioglio, C. M. Wolff, O. J. Sandberg, A. Armin, B. Rech, S. Albrecht, D. Neher, M. Stolterfoht, On the origin of the ideality factor in perovskite solar cells. *Adv. Energy Mater.* **10**, 2000502 (2020).

45. J. Nelson, "Ch. 4 Generation and recombination" in *The Physics of Solar Cells* (Imperial College, 2003), p. 79.

46. T. Kirchartz, U. Rau, What makes a good solar cell? *Adv. Energy Mater.* **8**, 1703385 (2018).

47. S. Wang, W. B. Xiao, F. Wang, Structural, electronic, and optical properties of cubic formamidinium lead iodide perovskite: A first-principles investigation. *RSC Adv.* **10**, 32364–32369 (2020).

48. R. H. Bube, "Ch. 2 Photoconductivity parameters" in *Photoelectronic Properties of Semiconductors* (Cambridge Univ., 1992), p.19.

49. S. Heo, G. Seo, Y. Lee, D. Lee, M. Seol, J. Lee, J. B. Park, K. Kim, D. J. Yun, Y. S. Kim, J. K. Shin, T. K. Ahn, M. K. Nazeeruddin, Deep level trapped defect analysis in $CH_3NH_3PbI_3$ perovskite solar cells by deep level transient spectroscopy. *Energ. Environ. Sci.* **10**, 1128–1133 (2017).

50. C. W. Warren, E. T. Roe, D. W. Miller, W. N. Shafarman, M. C. Lonergan, An improved method for determining carrier densities via drive level capacitance profiling. *Appl. Phys. Lett.* **110**, 203901 (2017).

51. M. A. Lampert, Volume-controlled current injection in insulators. *Rep. Prog. Phys.* **27**, 329–367 (1964).

52. V. M. Le Corre, E. A. Duijnstee, O. El Tambouli, J. M. Ball, H. J. Snaith, J. Lim, L. J. A. Koster, Revealing charge carrier mobility and defect densities in metal halide perovskites via space-charge-limited current measurements. *ACS Energy Lett.* **6**, 1087–1094 (2021).

53. R. R. Haering, E. N. Adams, Theory and application of thermally stimulated currents in photoconductors. *Phys. Rev.* **117**, 451–454 (1960).

54. A. Baumann, S. Väth, P. Rieder, M. C. Heiber, K. Tvingstedt, V. Dyakonov, Identification of trap states in perovskite solar cells. *J. Phys. Chem. Lett.* **6**, 2350–2354 (2015).

55. R. Brenes, D. Guo, A. Osherov, N. K. Noel, C. Eames, E. M. Hutter, S. K. Pathak, F. Niroui, R. H. Friend, M. Saiful Islam, H. J. Snaith, V. Bulović, T. J. Savenije, S. D. Stranks, Metal halide perovskite polycrystalline films exhibiting properties of single crystals. *Joule* **1**, 155–167 (2017).